Nanoscale

RSC Publishing

PAPER

View Article Online
View Journal | View Issue

Aqueous phase synthesis of upconversion nanocrystals through layer-by-layer epitaxial growth for *in vivo* X-ray computed tomography†

Cite this: *Nanoscale*, 2013, **5**, 6950

Feifei Li,[a] Chunguang Li,[a] Jianhua Liu,[b] Xiaomin Liu,[c] Lan Zhao,[d] Tianyu Bai,[a] Qinghai Yuan,[b] Xianggui Kong,[c] Yu Han,[d] Zhan Shi*[a] and Shouhua Feng[a]

Lanthanide-doped core–shell upconversion nanocrystals (UCNCs) have tremendous potential for applications in many fields, especially in bio-imaging and medical therapy. As core–shell UCNCs are mostly synthesized in organic solvents, tedious organic–aqueous phase transfer processes are usually needed for their use in bio-applications. Herein, we demonstrate the first example of one-step synthesis of highly luminescent core–shell UCNCs in the "aqueous" phase under mild conditions using innocuous reagents. A microwave-assisted approach allowed for layer-by-layer epitaxial growth of a hydrophilic $NaGdF_4$ shell on $NaYF_4$:Yb, Er cores. During this process, surface defects of the nanocrystals could be gradually passivated by the homogeneous shell deposition, resulting in obvious enhancement in the overall upconversion emission efficiency. In addition, the up-down conversion dual-mode luminescent $NaYF_4$:Yb, Er@$NaGdF_4$:Ce, Ln (Eu, Tb, Sm, Dy) nanocrystals were also synthesized to further validate the successful formation of the core–shell structure. More significantly, based on their superior solubility and stability in water solution, high upconversion efficiency and Gd-doped predominant X-ray absorption, the as-prepared $NaYF_4$:Yb, Er@$NaGdF_4$ core–shell UCNCs exhibited high contrast in *in vitro* cell imaging and *in vivo* X-ray computed tomography (CT) imaging, demonstrating great potential as multiplexed luminescent biolabels and CT contrast agents.

Received 27th March 2013
Accepted 17th May 2013

DOI: 10.1039/c3nr01530k

www.rsc.org/nanoscale

1 Introduction

A major challenge in diagnostic medicine and *in vivo* applications is to develop new imaging probes and technologies that enable the monitoring of physiological procedures in living cells, tissues, and organisms with high temporal and spatial resolutions.[1–6] Biological researchers are playing an important role in designing and fabricating novel imaging probes for application in diagnostic assays. Over the past decade, quantum dots (QDs) have been studied extensively because of their high extinction coefficient and quantum yield, easy tunability of emission wavelength, and resistance to photobleaching.[7–10] Fluorescent proteins have also been extensively used as bio-imaging agents due to their unique advantage of being able to be genetically expressed in specific cells.[11–15] Even so, the major obstacle in using them as imaging agents for long-term cellular imaging is that the visible/UV excitation can give rise to background autofluorescence signals, photobleaching and phototoxicity. Intense research has been fueled by the need for practical, robust and highly sensitive detection agents that can address the deficiencies of conventional technologies. Compared to conventional luminescent materials such as organic fluorescent dyes and QDs, lanthanide (Ln^{3+})-doped, near-infrared (NIR)-excited, upconversion labels show superior features, including sharp emission bandwidths (<10 nm), large anti-Stokes shifts (up to 500 nm), long luminescence lifetime (μs–ms range), high chemical stability and low long-term toxicity.[16–20] These features coupled with the remarkable light penetration depth and the absence of autofluorescence in biological specimens under infrared excitation make these upconversion nanocrystals (UCNCs) ideal luminescent probes for biological labeling and imaging.[21–25]

However, the low upconversion efficiency of UCNCs cannot satisfy the inherent requirement of a low excitation density level in biological systems.[26–29] To improve the upconversion luminescent intensity, the growth of a crystalline shell of a suitable

[a]*State Key Laboratory of Inorganic Synthesis and Preparative Chemistry, College of Chemistry, Jilin University, Changchun 130012, P.R. China. E-mail: zshi@mail.jlu.edu.cn; Fax: +86 431 85168624*

[b]*Department of Radiology, The Second Hospital of Jilin University, Changchun 130022, P.R. China*

[c]*State Key Laboratory of Luminescence and Applications, Changchun Institute of Optics, Fine Mechanics and Physics, Chinese Academy of Sciences, Changchun 130033, P.R. China*

[d]*Advanced Membrane and Porous Materials Center & Imaging and Characterization Core Lab, King Abdullah University of Science and Technology, Thuwal 23955-6900, Saudi Arabia*

† Electronic supplementary information (ESI) available: FT-IR, XPS, excitation spectra of $NaYF_4$:Yb, Er@$NaGdF_4$:Ce, Ln core–shell UCNC *in vivo* imaging, CT images of a rat before and after intravenous injection of Iobitridol, CT values. See DOI: 10.1039/c3nr01530k

inorganic material around each nanocrystal (NC) to form the core–shell structure has proved to be an effective strategy.[30–36] In recent years, the synthesis of core–shell structural materials with luminescent lanthanide NCs as cores and inert host compounds as shells has been reported by several groups.[37] Lately, $NaGdF_4$:Yb, Er@$NaGdF_4$:Yb nanoparticles with a core–active-shell structure were prepared by Capobianco's group.[38] The active shell seemed more effective in enhancing the upconversion efficiency in comparison with inert shells. Van Veggel and co-workers[39] demonstrated a novel epitaxial layer-by-layer growth on $NaYF_4$ NCs utilizing Ostwald ripening dynamics to tune both shell thickness and composition. Zhao's group[40] has established a strong linear link between the $NaGdF_4$ shell thickness and the optical response of the hexagonal $NaYF_4$:Yb, Er@$NaGdF_4$ core–shell NCs. To date, almost all of the core–shell UCNCs were obtained in the "organic" phase, mainly based on the decomposition of trifluoroacetate precursors in organic reagents. This method has some drawbacks, such as rigorous experimental conditions, hazardous precursors, and toxic solvents. Particularly, complicated surface modification processes are needed to make the as-synthesized nanocrystals water soluble and bio-compatible.

Our group has recently successfully prepared monodisperse hydrophilic Ln^{3+}-doped $NaGdF_4$ UCNCs as multifunctional bioprobes *via* a microwave-assisted method.[41] Advancing a step, we here report for the first time layer-by-layer epitaxial growth of core–shell UCNCs in the aqueous phase under mild conditions using innocuous reagents. In particular, we synthesized highly water-soluble $NaYF_4$:Yb, Er@$NaGdF_4$ multilayer core–shell UCNCs by a microwave-assisted route with a polyol process. $NaYF_4$:Yb, Er nanocrystals with a mean size of 16.30 ± 0.80 nm were used as seeds for the epitaxial growth, while precise enhancement of the UC optical intensity was achieved by varying the thickness of the $NaGdF_4$ shell. Polyethylenimine (PEI) was used as a capping agent not only to enhance UC fluorescence intensity but also to keep these NCs well dispersed in various hydrophilic solvents.[42] The near-infrared to visible UC luminescence of the UCNCs can effectively avoid the *in vitro* cell damage and weak penetration associated with the UV excitation. More significantly, the Gd-based shell contains Gd which well matches with the X-ray photon energy and thus the Gd-based UCNCs can be used in clinical applications. We demonstrate that these UCNCs can act as high-performance CT contrast agents with long circulation time and low toxicity for *in vivo* angiography and bimodal image-guided lymph node mapping.

2 Experimental

2.1 Chemicals

High purity (99.9%) $GdCl_3$, $YCl_3 \cdot 6H_2O$, $ErCl_3 \cdot 6H_2O$, $YbCl_3 \cdot 6H_2O$, $TbCl_3 \cdot 6H_2O$, $EuCl_3 \cdot 6H_2O$, $DyCl_3 \cdot 6H_2O$, $SmCl_3 \cdot 6H_2O$, and polyethylenimine branched [PEI, $M_w = 25\,000$] were purchased from Sigma-Aldrich, Ltd. $Ce(NO_3)_3 \cdot 6H_2O$, NH_4F (96%), NaCl (99%), and ethylene glycol (99%) were purchased from Sinopharm Chemical Reagent Co. Ltd. Unless otherwise noted, all chemicals were used as received without further purification.

2.2 Animal imaging

Animal care and handling procedures were in agreement with the guidelines of the Regional Ethics Committee for Animal Experiments.

2.3 Synthesis of $NaYF_4$:20%Yb, 2%Er core nanocrystals

A commercial microwave reactor (ETHOS ONE, ITALY) system was used to synthesize $NaYF_4$:Yb, Er nanocrystals. In a typical procedure, a 0.468 mmol portion of $YCl_3 \cdot 6H_2O$, $YbCl_3 \cdot 6H_2O$ (0.12 mmol), $ErCl_3 \cdot 6H_2O$ (0.012 mmol), NaCl (0.6 mmol) and PEI (0.15 g) were dissolved in ethylene glycol (9 mL) at room temperature under stirring to form a homogeneous solution. Then, NH_4F (2.4 mmol) dissolved in ethylene glycol (6 mL) (also at the same temperature) was injected into the reaction mixture with stirring. The mixture solution was transferred to the reacting vessel of a microwave reactor, heated to 200 °C for 10 min by microwave irradiation with the power of 400 W and then cooled to room temperature naturally. The product was isolated by centrifugation at 11 000 rpm for 10 min, washed with deionized water and ethanol in sequence, and redispersed in deionized (DI) water (3 mL) to form a transparent colloidal solution.

2.4 Synthesis of $NaYF_4$:20%Yb, 2%Er@$NaGdF_4$ core–shell nanocrystals with a 1-layer $NaGdF_4$ shell by a one-step coating procedure

The core upconversion NCs were synthesized as described above and used as seeds for the core–shell reaction. A commercial microwave reactor system was used to synthesize $NaYF_4$:20%Yb, 2%Er@$NaGdF_4$ 1-layer core–shell nanocrystals. In a typical procedure, a 0.3 mmol portion of $NaYF_4$:20%Yb, 2% Er core nanocrystals in ethylene glycol (1.5 mL), $GdCl_3$ (0.1 mmol), NaCl (0.1 mmol) and PEI (0.15 g) were dissolved in ethylene glycol (9 mL) at room temperature under stirring to form a homogeneous solution. Then, NH_4F (0.4 mmol) dissolved in ethylene glycol (6 mL) (also at the same temperature) was injected into the reaction mixture. The mixture solution was transferred to the reacting vessel of a microwave reactor, heated to 200 °C for 10 min by microwave irradiation and then cooled to room temperature naturally. The 1-layer $NaYF_4$:20% Yb, 2%Er@$NaGdF_4$ core–shell NCs were precipitated and washed as described above and dispersed in DI water (3 mL).

2.5 Synthesis of $NaYF_4$:20%Yb, 2%Er@$NaGdF_4$ core–shell nanocrystals with a 2-layer $NaGdF_4$ shell

The 1-layer $NaYF_4$:20%Yb, 2%Er@$NaGdF_4$ core–shell NCs were synthesized as described above and used as seeds for the 2-layer core–shell reaction. A commercial microwave reactor system was used to synthesize the 2-layer $NaYF_4$:20%Yb, 2% Er@$NaGdF_4$ core–shell nanocrystals. In a typical procedure, a 0.3 mmol portion of 1-layer $NaYF_4$:20%Yb, 2%Er@$NaGdF_4$ core–shell NCs in ethylene glycol (1.5 mL), $GdCl_3$ (0.2 mmol), NaCl (0.2 mmol) and PEI (0.15 g) were dissolved in ethylene glycol (9 mL) at room temperature under stirring to form a homogeneous solution. Then NH_4F (0.8 mmol) dissolved in ethylene glycol (6 mL) (also at the same temperature) was

injected into the reaction mixture. The mixture solution was transferred to the reacting vessel of a microwave reactor, heated to 200 °C for 10 min by microwave irradiation and then cooled to room temperature naturally. The 2-layer $NaYF_4$:20%Yb, 2% Er@$NaGdF_4$ core–shell NCs were precipitated and washed as described above and dispersed in DI water (3 mL).

2.6 Synthesis of $NaYF_4$:20%Yb, 2%Er@$NaGdF_4$ core–shell nanocrystals with a 3-layer $NaGdF_4$ shell

The 2-layer $NaYF_4$:20%Yb, 2%Er@$NaGdF_4$ core–shell NCs were synthesized as described above and used as seeds for the 3-layer core–shell reaction. In a typical procedure, a 0.3 mmol portion of 2-layer $NaYF_4$:20%Yb, 2%Er@$NaGdF_4$ core–shell NCs in ethylene glycol (1.5 mL), $GdCl_3$ (0.3 mmol), NaCl (0.3 mmol) and PEI (0.15 g) were dissolved in ethylene glycol (9 mL) at room temperature under stirring to form a homogeneous solution. NH_4F (1.2 mmol) dissolved in ethylene glycol (6 mL) (also at the same temperature) was then injected into the reaction mixture. The mixture solution was transferred to the reacting vessel of a microwave reactor, heated to 200 °C for 10 min by microwave irradiation and then cooled to room temperature naturally. The 3-layer $NaYF_4$:20%Yb, 2%Er@$NaGdF_4$ core–shell NCs were precipitated and washed as described above and dispersed in DI water (3 mL).

2.7 Synthesis of $NaYF_4$:20%Yb, 2%Er@$NaGdF_4$ core–shell nanocrystals with a 4-layer $NaGdF_4$ shell

The 3-layer $NaYF_4$:20%Yb, 2%Er@$NaGdF_4$ core–shell NCs were synthesized as described above and used as seeds for the 4-layer core–shell reaction. In a typical procedure, a 0.3 mmol portion of 3-layer $NaYF_4$:20%Yb, 2%Er@$NaGdF_4$ core–shell NCs in ethylene glycol (1.5 mL), $GdCl_3$ (0.4 mmol), NaCl (0.4 mmol) and PEI (0.15 g) were dissolved in ethylene glycol (9 mL) at room temperature under stirring to form a homogeneous solution. Then, NH_4F (1.6 mmol) dissolved in ethylene glycol (6 mL) (also at the same temperature) was injected into the reaction mixture. The mixture solution was transferred to the reacting vessel of a microwave reactor, heated to 200 °C for 10 min by microwave irradiation and then cooled to room temperature naturally. The 4-layer $NaYF_4$:20%Yb, 2%Er@$NaGdF_4$ core–shell NCs were precipitated and washed as described above and dispersed in DI water (3 mL).

2.8 Synthesis of $NaYF_4$:20%Yb, 2%Er@$NaGdF_4$:Ce, Ln core–shell nanocrystals with a 1-layer $NaGdF_4$:Ce, Ln shell

The core upconversion NCs were synthesized as described above and used as seeds for the $NaYF_4$:20%Yb, 2% Er@$NaGdF_4$:Ce, Ln (Ln = Tb, Eu, Sm, Dy) core–shell reaction. A commercial microwave reactor system was used. The doping ratio of Ce : Tb, Ce : Sm, Ce : Dy and Ce : Eu was 15% : 5%, 15% : 5%, 15% : 5% and 2.5% : 2.5%, respectively. In a typical procedure, a (0.3 mmol) portion of $NaYF_4$:20%Yb, 2%Er core nanocrystals in ethylene glycol (1.5 mL), $GdCl_3$ (0.08 mmol), NaCl (0.1 mmol), $Ce(NO_3)_3 \cdot 6H_2O$ (0.015 mmol), $TbCl_3 \cdot 6H_2O$ (0.005 mmol) and PEI (0.15 g) were dissolved in ethylene glycol (9 mL) at room temperature under stirring to form a homogeneous solution. Then, NH_4F (0.4 mmol) dissolved in ethylene glycol (6 mL) (also at the same temperature) was injected into the reaction mixture. The mixture solution was transferred to the reacting vessel of a microwave reactor, heated to 200 °C for 10 min by microwave irradiation and then cooled to room temperature naturally. The 1-layer $NaYF_4$:20%Yb, 2% Er@$NaGdF_4$:15% Ce, 5% Tb core–shell NCs were precipitated and washed as described above and dispersed in DI water (3 mL). Other $NaYF_4$:20%Yb, 2%Er@$NaGdF_4$:Ce, Ln (Ln = Eu, Sm, Dy) core–shell NCs were prepared by a similar procedure, except that $Ce(NO_3)_3 \cdot 6H_2O$ and $TbCl_3 \cdot 6H_2O$ were replaced by the corresponding doping concentration.

2.9 Cell culture and *in vivo* cellular imaging

The viability and proliferation of cells were evaluated by the well-known methyl thiazolyl tetrazolium (MTT) assay. HeLa cell lines were provided by the Department of Immunology, Norman Bethune College of Medicine, Jilin University. The HeLa cells were maintained in modified Dulbecco's Modified Eagle Media (DMEM) supplemented with 10% heat-inactivated fetal bovine serum (Sigma) 100 μg mL^{-1} streptomycin and 100 IU mL^{-1} penicillin (Invitrogen). The cells were maintained at 37 °C in a 5% CO_2 incubator. The cytotoxicity of the complexes was evaluated by MTT reduction assays. HeLa cells were seeded in 96-well plates (Coster, MA, USA) at 1.2 × 104 per well in growth medium (100 μL). The cells were incubated at 37 °C in a 5% CO_2 atmosphere for 24 h. Then the cells were treated with various concentrations of complexes in a mixture of growth medium. Finally, the cells were incubated at 37 °C in a 5% CO_2 atmosphere for 12 h and 24 h. At each time point, viable cells were evaluated by using MTT assays. 20 μL MTT (final concentration 5 mg mL^{-1}) was added to each well, and then the plates were further incubated for 4 h, after which MTT was removed and the water-insoluble formazan was dissolved by adding 200 μL DMSO to each well. The optical density (OD) was measured using an absorbance microplate reader TQuant (BioTEK, USA) at a wavelength of 490 nm. The error bar represents one standard deviation. The results shown are a cumulative analysis of 3 wells per group. Cellular imaging was performed using a Motic AE31 microscope equipped with an Andor GNIR CCD camera (iXon3 888-BV), which is capable of imaging in the range of 500–850 nm. A fiber coupled laser diode (nlight, NL-PPS50) emitting at 980 nm was used as the light source, and the fiber was introduced through the entrance port of the microscope. The emitted light was passed through a 900 nm short-wave pass filter and recorded using a CCD camera.

2.10 CT imaging

To assess CT contrast efficacy, $NaYF_4$:20%Yb, 2%Er UCNCs, $NaYF_4$:20%Yb, 2%Er@$NaGdF_4$ core–shell UCNCs or Iobitridol were dispersed in water, respectively. For *in vivo* CT imaging, the rat was first anesthetized by intraperitoneal injection of chloral hydrate solution (10 wt%), and then 1 mL of $NaYF_4$:20%Yb, 2% Er@$NaGdF_4$ core–shell UCNC solution (420 Gd mg mL^{-1}) or 0.3 mL of Iobitridol (the most widely used in clinical applications, 350 Iobitridol mg mL^{-1}) were injected intravenously into

two rats, respectively. CT images were collected using a JL U.A NO.2 HOSP Philips iCT 256 slice scanner. Imaging parameters were as follows: thickness, 0.9 mm; pitch, 0.99; 120 kVp, 300 mA; field of view, 350 mm; gantry rotation time, 0.5 s; table speed, 158.9 mm s^{-1}.

2.11 Characterization

TEM and HRTEM were performed on a FEI Tecnai G2 S-Twin with a field emission gun operating at 200 kV. The FEI Tecnai G2 S-Twin was equipped with an EDS detector, which was used for elemental analysis of the nanocrystal composition. High-resolution STEM was performed on an FEI aberration-corrected Titan Cubed S-Twin transmission electron microscope operating at 200 kV. A probe Cs corrector was applied to get better spatial resolution. In a typical experiment, high-resolution STEM imaging was conducted at a 2 μs per pixel scanning rate with a 70 μm C2 aperture, spot size 9, a high-angle annular dark-field (HAADF) detector, and 146 mm camera length. Under such conditions a spatial resolution of ~1.0 Å was obtained. Images were acquired digitally on a Gantan multiple CCD camera. XRD analysis was performed on a Rigaku D/max-2500 diffractometer with a graphite monochromator by using Cu Kα radiation operating at 200 mA and 40 kV. XRD data were collected over the range of 20–70° (2θ) with a step interval of 0.02° and a preset time of 1.6 s per step at room temperature. The IR spectra were acquired on a Bruker IFS 66v/S FTIR spectrometer. The surface of nanocrystals was characterized by X-ray photoelectron spectroscopy (XPS), the spectra were collected on an ESCALAB 250 X-ray photoelectron spectroscope using Mg Kα X-ray as the excitation source. The photoluminescence (PL) spectra were recorded on an Edinburgh Instruments FLS920 spectrofluorimeter using an external 0–600 mW adjustable continuous wave 980 nm laser as the excitation source. The luminescence kinetics was recorded with a 500 MHz Tektronix digital oscilloscope and the excitation was realized by a nanosecond pulse train at 980 nm from an optical parametric oscillator. The magnetic properties of the samples were evaluated by means of an MPMS-XL superconducting quantum interference device (SQUID) magnetometer.

3 Results and discussion

3.1 Synthesis and characterization of layer-by-layer UCNCs

$NaYF_4$:20%Yb, 2%Er core and $NaYF_4$:20%Yb, 2%Er core overcoated with layer-by-layer $NaGdF_4$ shell UCNCs were synthesized *via* an efficient and environmentally friendly microwave-accelerated procedure. PEI molecules were used as a surfactant to stabilize Ln^{3+} ions and subsequently control the growth of NCs upon addition of fluoride ions. Moreover, the PEI-coated UCNCs provide a platform for the UCNCs to be well-dispersed in various hydrophilic solvents including water, ethanol, dimethylformamide, dimethylsulphoxide, ethylene glycol and so on. PEI was a thermally stable and hydrophilic polymer with primary, secondary and tertiary amino groups, which rendered the nanoparticles water-soluble. The amino groups could not only help to improve the UC fluorescence intensity but also be used for conjugation of biomolecules to the nanoparticles.[25a,29]

From the FT-IR spectra (Fig. S1 in the ESI†), an intense amino absorption band in the region of 1380–1630 cm^{-1} can be observed, indicative of positively charged PEI on the surface of $NaYF_4$:Yb, Er@$NaGdF_4$ core–shell UCNCs. We began with an ethanol solution of pre-synthesized $NaYF_4$:20%Yb, 2%Er core UCNCs and successively deposited the second shell of $NaGdF_4$, then the next $NaGdF_4$ shell through an epitaxial growth process. Notably, the layer-by-layer growth process has also been extensively investigated by the groups of Liu, Yan, Zhang, Wang, and Chow *et al.*[43–47]

Herein, we describe the first example of water-soluble one-step synthesis of multishell spherical UCNCs. Fig. 1a–d show the transmission electron microscopy (TEM) images of the resulting UCNCs before and after the shell growth. As one can see in Fig. 1a and b, the $NaYF_4$:Yb, Er (20/2%) core UCNCs were nearly spherical in shape, which were confirmed to be single crystals by high-resolution TEM (Fig. 1b, inset). Histograms of the size distribution of the core UCNCs are shown in the inset of Fig. 1a, with an average diameter of about 16.3 nm. Fig. 1c and d show representative TEM images of synthesized $NaYF_4$:Yb, Er@$NaGdF_4$ core–shell UCNCs. It is obvious that the diameter of the core–shell UCNCs increased to about 23.8 nm after growth of the $NaGdF_4$ layer and the uniformity of size and shape remained almost unchanged. The size increase of the core–shell NCs along with highly uniform morphology suggests that the $NaGdF_4$ shell was grown on the surface of $NaYF_4$:Yb, Er core UCNCs. Lattice fringes corresponding to the (111) planes of cubic-phase $NaYF_4$ can be observed in the high-resolution transmission electron microscopic (HRTEM) image (Fig. 1d, inset), suggesting the highly crystalline nature of the core–shell UCNCs. The highly crystalline core and core–shell UCNCs can be further confirmed by the X-ray powder diffraction (XRD) analysis. The selected area electron diffraction (SAED) patterns shown as insets of Fig. 1a and c demonstrate that the $NaYF_4$:Yb, Er core UCNCs and the $NaYF_4$:Yb, Er@$NaGdF_4$ core–shell UCNCs are both of cubic phases and can be indexed to the JCPDS 06-0342 cubic $NaYF_4$ structure.

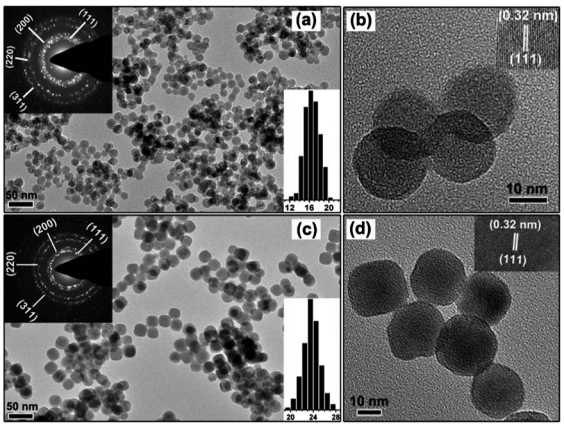

Fig. 1 TEM images of $NaYF_4$:Yb, Er core (a–b) and 3-layer $NaYF_4$:Yb, Er@$NaGdF_4$ UCNCs (c–d) at different magnifications. Insets in (a) and (c) display histograms of the size distribution and SAED patterns of $NaYF_4$:Yb, Er core and 3-layer $NaYF_4$:Yb, Er@$NaGdF_4$ UCNCs, respectively. Insets in (b) and (d) are their corresponding HRTEM images.

To determine precisely the effects of shell thickness on the optical properties of the resulting UCNCs, monolayer control of shell thickness must be achieved. In order to realize these goals, we first synthesized $NaYF_4$:Yb, Er cores with the mean size of 16.30 ± 0.80 nm. Epitaxial growth of the first layer (1^{st}: $NaGdF_4$), denoted as 1-layer, then the second layer (2^{nd}: $NaGdF_4$, 2-layer), the third layer (3^{rd}: $NaGdF_4$, 3-layer) and the fourth layer (4^{th}: $NaGdF_4$, 4-layer) was achieved by a seeded re-growth process. The seeded re-growth cycle can be repeated multiple times to generate layer-by-layer shell growth. Fig. 2a–e and Fig. 2f–j show the low and high magnification TEM images of monodispersed core and core–shell models. The images demonstrate the easy control offered by this method in tuning shell thickness, which was achieved by four successive increases in the amount of shell's injection and ripening cycles. In more detail, the amount of the $NaGdF_4$ was 0.1 mmol, 0.2 mmol, 0.3 mmol, 0.4 mmol in the preparation of core–shell UCNCs from the first layer to the fourth layer, respectively. Therefore, the $NaGdF_4$ shell-thicknesses in a newly designed model ($NaYF_4$:20%Yb, 2% Er@$NaGdF_4$$\cdots$@$NaGdF_4$) were carefully tuned from 2.2 nm to 14.3 nm by changing the amount of shell precursors. With the increase of the $NaGdF_4$ shell, core–shell UCNCs' size growth was evidenced from the TEM images of the same magnification (Fig. 2a–e). It was revealed that in all cases the standard deviations of the UCNC size distributions were all about 0.8 nm. In addition, as we can see from Fig. 2a–j, the shape of the core–shell UCNCs changed from spherical to cubic with the increase of the shell layers.

X-ray photoelectron spectroscopy (XPS) further provides the surface information of core–shell UCNCs (Fig. S2 in the ESI†). The XRD pattern of $NaYF_4$:Yb, Er core UCNCs can be indexed to a cubic phase of the bulk $NaYF_4$ crystal (Fig. 2k), which corresponds to the SAED patterns. Both the XRD and SAED data demonstrate that the shells grew in an epitaxial manner. Upon layer by layer growth of the $NaGdF_4$ shell, the diffraction peaks became broader and shifted toward lower angles to approach the values of a bulk $NaGdF_4$ crystal, consistent with the major change of UCNCs from the $NaYF_4$ core to $NaGdF_4$ shell.[48] More importantly, we also observed that the cubic-to-hexagonal phase transformation was further confirmed by the increase in shell thickness. This phase conversion was very beneficial for the enhancement of UC fluorescence intensity. Fig. 2 shows the HRTEM image of a single 4-layer nanocrystal with a square shape. Obviously, the 4-layer core–shell UCNC grew up on the basis of the 3-layer core–shell UCNC. In combination with scanning transmission electron microscopy (STEM) (Fig. 2m), energy dispersive X-ray spectroscopy (EDS) (Fig. 2n) studies have proven to be advantageous in the research of core–shell nanostructures. EDS revealed the presence of the main elemental Y, Gd, Yb and Er in 4-layer $NaYF_4$:Yb, Er@$NaGdF_4$ core–shell UCNCs, further confirming that our method can control the shell-thickness of water-soluble layer-by-layer $NaYF_4$:Yb, Er@$NaGdF_4$ core–shell UCNCs.

3.2 Shell thickness dependence of UC optical and dual-mode PL properties

The consistent increase in upconversion emission intensity of both green and red emissions with increasing layer thickness with the optically active ion concentration (Yb^{3+}, Er^{3+}) remaining constant further confirmed the epitaxial shell growth. The effect of shell thickness on the UC optical properties of the $NaYF_4$:Yb, Er@$NaGdF_4$ core–shell UCNCs is plotted in Fig. 3. Upon deposition of the 1-layer $NaYF_4$:Yb, Er@$NaGdF_4$ core–shell UCNCs, an increase in the intensity and lifetime was observed (Fig. 3a–e), indicative of epitaxial surface passivation and increased electronic isolation of the core from its environment. Ideally, a uniform shell should be formed over UCNCs

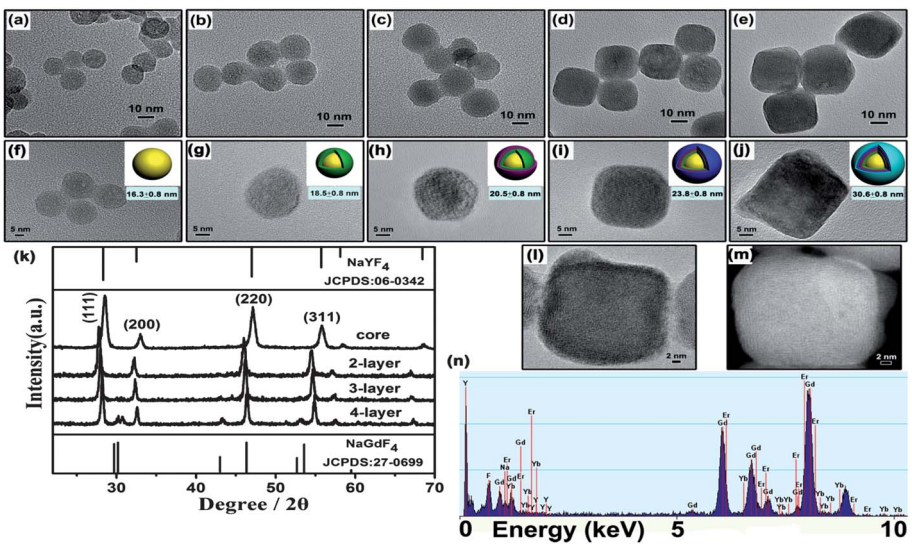

Fig. 2 (a–e) TEM images of the $NaYF_4$:Yb, Er core and those overcoated with 1–4 layers of the $NaGdF_4$ shell, respectively. (f–j) HRTEM images and their corresponding 3D schematic diagram of the $NaYF_4$:Yb, Er core and those overcoated with 1–4 layers of the $NaGdF_4$ shell, respectively. (k) XRD patterns of $NaYF_4$:Yb, Er core and the corresponding core–shell UCNCs. (l–m) HRTEM and HADDF-STEM images of a single 4-layer $NaYF_4$:Yb, Er@$NaGdF_4$ UCNC. (n) EDS of the 4-layer $NaYF_4$:Yb, Er@$NaGdF_4$ UCNCs.

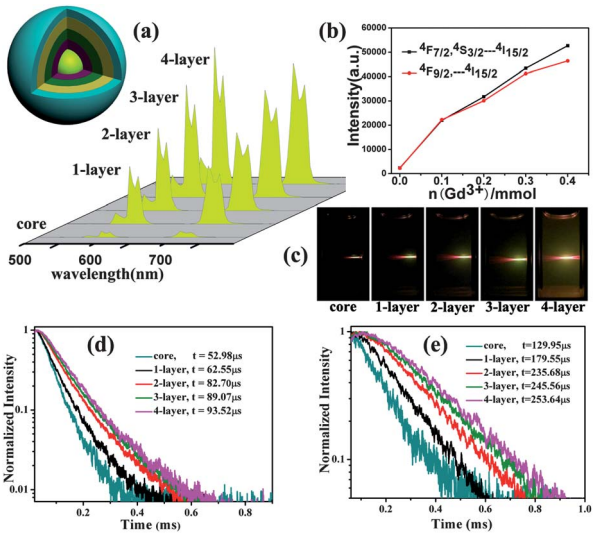

Fig. 3 Room-temperature UC luminescence spectra (a), evolution statistics (b), and photographs of colloidal solutions (c) of ethanol solutions comprising $NaYF_4$:Yb, Er core UCNCs and the corresponding core–shell UCNCs with 1–4 layers of the $NaGdF_4$ shell under excitation with a 980 nm laser. (d–e) UC luminescence decay curves of $NaYF_4$:Yb, Er core UCNCs and the corresponding core–shell UCNCs with 1–4 layers of the $NaGdF_4$ shell.

after the deposition of every layer. Any voids on the surface can affect the photostability and also induce the leakage of the core material. During the epitaxial and layer-by-layer growth of the $NaGdF_4$ shell, surface defects of the UCNCs can be gradually passivated, resulting in the obvious enhancement in overall UC luminescence emission (Fig. 3a and c). Under the excitation of an NIR laser ($\lambda = 980$ nm) with identical laser power 200 mW, the probe showed obviously increased green emission by gradually increasing the shell thickness (Fig. 3c). Upon continuous shell growth, a linear increase in intensity (Fig. 3b) was observed. The improvement of the luminescent intensity was further verified by the temporal behaviour of upconversion luminescence of core and core–shell UCNCs with different shell thickness recorded at 540 and 650 nm (Fig. 3d and e). With the increase of the layers of $NaGdF_4$, it was observed that the upconversion luminescence decay time in Fig. 3d and e significantly increased, besides the luminescence enhancement shown in Fig. 3a.

To further prove the feasibility of the layer-by-layer $NaYF_4$:Yb, Er@$NaGdF_4$ core–shell structure in the aqueous phase, we also carried out a series of up-down conversion dual-mode luminescence of $NaYF_4$:Yb, Er@$NaGdF_4$:Ce, Ln (Ln = Eu, Tb, Sm, Dy) core–shell coating experiments. It should be mentioned that relatively high activator concentrations (Ce : Ln concentration ratio was 15% : 15% for Ln = Tb, Sm, or Dy; 2.5% : 2.5% for Ln = Eu) were optimal doping ratios to give rise to strong fluorescence emissions.[49,50] Fig. 4a shows the emission spectra of the $NaYF_4$:Yb, Er core UCNCs and $NaYF_4$:Yb, Er@$NaGdF_4$:Ce, Ln (Ln = Eu, Tb, Sm, Dy) core–shell NCs in aqueous solutions. As shown in Fig. S3 in the ESI,† the excitation spectra of all the samples consisted of a broad band at around 264 nm, which was ascribed to the Ce^{3+} 4f–5d transition. The other sharp lines in each emission spectrum (Fig. 4a) were attributed to the characteristic optical transitions of the corresponding luminescent ions. The black squares indicate Commission Internationale de l'Eclairage (CIE) chromaticity coordinate positions. As illustrated in Fig. 4b, the black squares indicate that the CIE chromaticity coordinates for these samples fell in the green-yellow, red, green, pink and blue regions, respectively, which were consistent with the corresponding emission spectra and the photographs of these NCs (Fig. 4f). And the digital DC–UC dual-mode luminescence photos of the samples were achieved

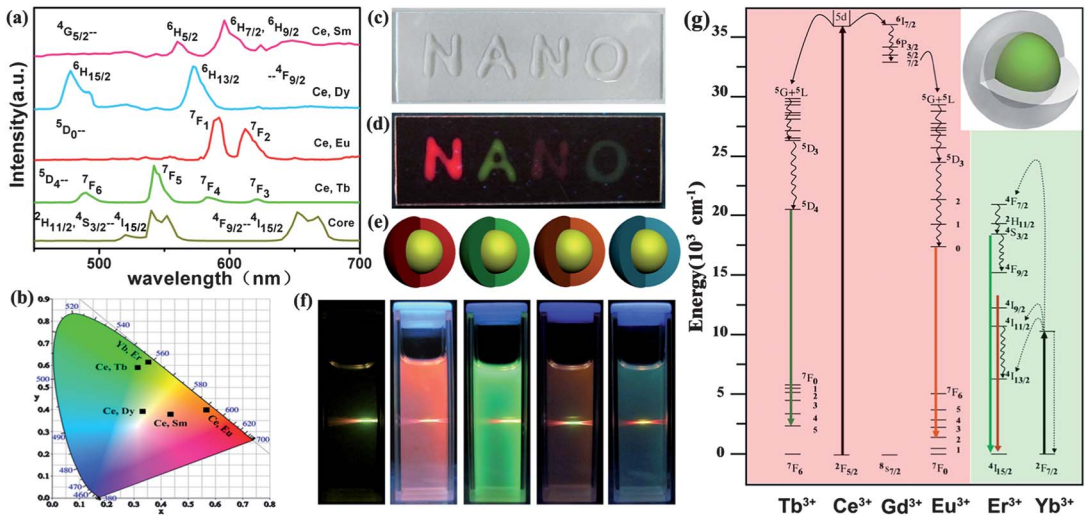

Fig. 4 (a) Room-temperature PL emission spectra of $NaYF_4$:Yb, Er and $NaYF_4$:Yb, Er@$NaGdF_4$:Ce, Ln core–shell NCs. (b) Corresponding Commission Internationale de l'Eclairage (CIE) chromaticity coordinates of the multicolour emissions from the samples shown in (a). (c) Photograph showing physical dimension and transparency of a PDMS sample composed of $NaYF_4$:Yb, Er@$NaGdF_4$:Ce, Ln core–shell NCs. (d–e) Their corresponding bright colour emission under 254 nm UV irradiation and 3D schematic diagram. (f) PL photos showing corresponding colloidal solutions of (a). (g) Energy level diagram and the excitation/emission pathways of the Ln^{3+} investigated. Only the predominantly observed emission pathways are highlighted. All of the samples' concentrations were 0.2 M. UC emission spectra were excited using a 600 mW 980 nm diode laser.

Table 1 The summary of composition, emission, emission colour and chromaticity coordinates (*x*, *y*) of the as-prepared $NaYF_4$:Yb, Er@$NaGdF_4$:Ce, Ln (Eu, Tb, Sm, Dy) core–shell NCs

Ln^{3+}	Emissions (nm)	Transitions	Colour	CIE (*x*,*y*)
Ce^{3+}, Sm^{3+}	560, 593–614, 642	$^4G_{5/2} \rightarrow {}^6H_{5/2,7/2,9/2}$	Pink	(0.438, 0.361)
Ce^{3+}, Dy^{3+}	480, 571	$^4F_{9/2} \rightarrow {}^6H_{15/2,13/2}$	Blue	(0.336, 0.383)
Ce^{3+}, Eu^{3+}	591, 615–625	$^5D_0 \rightarrow {}^7F_{1,2}$	Red	(0.557, 0.392)
Ce^{3+}, Tb^{3+}	490, 544, 584, 619	$^5D_4 \rightarrow {}^7F_{6,5,4,3}$	Green	(0.307, 0.577)
Yb^{3+}, Er^{3+}	523, 542, 659	$^2H_{11/2}$, $^4S_{3/2} \rightarrow {}^4I_{15/2}$, $^4H_{9/2} \rightarrow {}^4I_{15/2}$	Green-yellow	(0.352, 0.622)

under both the 254 nm UV light and 980 nm laser excitation. This indicates that the construction of a dual-mode core–shell structure in the aqueous phase can be achieved. As a comparison, the assignments of these emissions, emission colour and chromaticity coordinates (*x*, *y*) are summarized in Table 1. In addition, multicolour emissions could be realized, which endowed this kind of material with potential applications in multiplexing detection and imaging.

Owing to their small feature size and ease of dispersion, these nanoparticles could readily be incorporated into polydimethylsiloxane (PDMS) monoliths to construct volumetric three-dimensional (3D) displays (Fig. 4c and d), presenting unique interface applications for 3D image visualization. In our previous report,[51] the introduction of nanoparticles into a polymer matrix has proved to be an effective method to improve the stability of the nanoparticles and the performance of the polymers. In this work, a stable and functionalized solid composite product was obtained by embedding the aqueous solution of $NaYF_4$:Yb, Er@$NaGdF_4$:Ce, Ln (Ln = Eu, Tb, Sm, Dy) core–shell NCs in a PDMS matrix. We could write four letters with the above four types of doping, which showed strong visible emission under UV irradiation. Fig. 4e shows 3D schematic models corresponding to the four types of core–shell letters. After curing, the composite film was very stable and flexible. It could be stretched lightly while still retaining photoluminescent character. Furthermore, we showed the schematic of the energy transfer mechanism of $NaYF_4$:Yb, Er@$NaGdF_4$:Ce, Ln (Ln = Eu, Tb, Sm, Dy) core–shell NCs (Fig. 4g).[52–54]

3.3 *In vitro* cell labeling and *in vivo* X-ray CT imaging

Apart from the aforementioned luminescence properties, the $NaYF_4$:Yb, Er@$NaGdF_4$ layer-by-layer core–shell UCNCs showed typical paramagnetism at room temperature because of the Gd in the samples (Fig. 5a). We compared the magnetic properties of one-layer core–shell UCNCs with those of four-layer core–shell UCNCs. The mass magnetic susceptibility of core–shell UCNCs increased from $9.50 \pm 0.01 \times 10^{-5}$ emu Oe^{-1} g^{-1} for 1-layer to $9.62 \pm 0.01 \times 10^{-5}$ emu Oe^{-1} g^{-1} for 4-layer according to the magnetization slope, which can be used for magnetic bioseparation. Prior to using $NaYF_4$:Yb, Er@$NaGdF_4$ layer-by-layer core–shell UCNCs for *in vivo* imaging, we first tested their cytotoxicity using the MTT assay. This crucial factor must be established in determining the suitability of this agent for specific applications in experimental small-animals and ultimately in clinical studies. To further prove the superiority of the

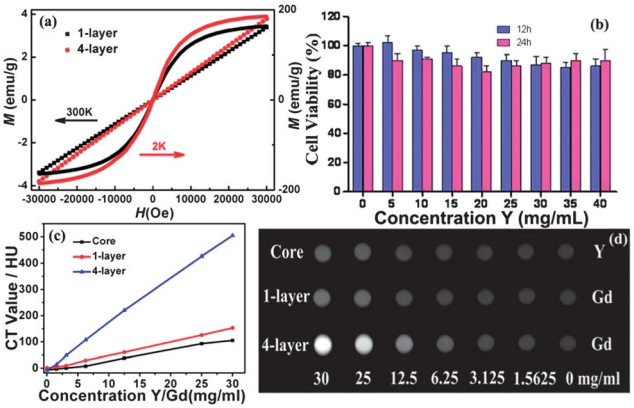

Fig. 5 (a) Magnetization curves of 1-layer and 4-layer $NaYF_4$:Yb, Er@$NaGdF_4$ core–shell UCNCs. (b) Cell viability of HeLa cells after incubation with increased concentration of 4-layer $NaYF_4$:Yb, Er@$NaGdF_4$ core–shell UCNCs for 24 h. (c) CT value (HU) of $NaYF_4$:Yb, Er core, 1-layer and 4-layer $NaYF_4$:Yb, Er@$NaGdF_4$ core–shell UCNCs as a function of the concentration of core (black trace) 1-layer (red trace) and 4-layer (blue trace), respectively. (d) CT images of solutions of $NaYF_4$:Yb, Er core, 1-layer and 4-layer $NaYF_4$:Yb, Er@$NaGdF_4$ core–shell UCNCs, respectively.

direct biological application of our water-soluble nanoparticles, the sample concentration was increased to a limit.[55,56]

Encouragingly, cell viability was not hindered by core–shell UCNCs up to a concentration of 40 mg mL^{-1} for *Y*, which revealed the remarkably low cytotoxicity of the core–shell UCNCs. Furthermore, we also investigated the behaviour of $NaYF_4$:Yb, Er core and $NaYF_4$:Yb, Er@$NaGdF_4$ layer-by-layer core–shell UCNCs in living cells. We cultured human cervical carcinoma HeLa cells in aqueous suspension containing a desired amount of the as-prepared UCNCs for 24 h and then investigated the *in vitro* imaging excited by 980 nm wavelength laser radiation. Interestingly, the as-prepared UCNCs without any surface-modification could enter the HeLa cells. Fig. 6 shows the multiphoton fluorescence microscopy image, the corresponding bright field image, the confocal fluorescence image and an overlay of the fluorescence microscopy image of HeLa cells after 24 h exposure to the UCNCs. It can be seen that UCNCs are localized in the cytoplasm of a number of HeLa cells with low toxicity for *in vitro* imaging. With 980 nm wavelength laser excitation, strong visible green emission can be observed in the cytoplasm of HeLa cells. As we know, the UCNCs have great advantages in biological imaging, because the use of NIR for excitation allows a greater penetration depth in biological

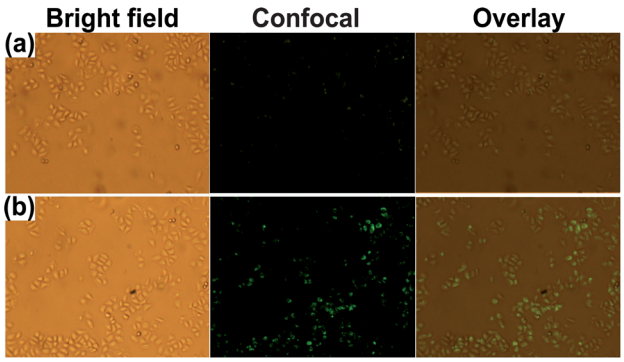

Fig. 6 Images of HeLa cells after growing with (a) $NaYF_4$:Yb, Er UCNCs, (b) 4-layer $NaYF_4$:Yb, Er@$NaGdF_4$ core–shell UCNCs for 24 h. Bright field images, confocal fluorescence images and superimposed images are shown, respectively.

tissues and results in lower phototoxicity and reduced background. To prove this, an aliquot (100 μL) of 4-layer core–shell UCNCs dispersed in water was subcutaneously injected into a Kunming mouse, and then a bright emission was clearly visible at the injection site. Fig. S4 in the ESI† demonstrates the potential value of core–shell UCNCs as luminescent probes for *in vivo* imaging.

Moreover, to assess CT contrast efficacy, we next compared the X-ray absorption between the 1-layer and the 4-layer $NaYF_4$:Yb, Er@$NaGdF_4$ core–shell UCNCs in solution. Both agents exhibited signal enhancement when the concentration of the agents was increased (Fig. 5c and d). A good linear correlation between the Hounsfield unit (HU) value and the concentration of Gd was observed. Nevertheless, at equivalent concentrations, the X-ray absorption of the 4-layer $NaYF_4$:Yb, Er@$NaGdF_4$ core–shell UCNCs was much higher than that of the 1-layer UCNCs (Fig. 5c). These results revealed that the as-prepared 4-layer $NaYF_4$:Yb, Er@$NaGdF_4$ core–shell UCNCs were greatly superior to other layers of $NaYF_4$:Yb, Er@$NaGdF_4$ core–shell UCNC *in vivo* CT contrast agents. These encouraging results prompted us to evaluate the feasibility of $NaYF_4$:Yb, Er@$NaGdF_4$ layer-by-layer core–shell UCNCs as *in vivo* CT imaging probes. A solution of 4-layer $NaYF_4$:Yb, Er@$NaGdF_4$ core–shell UCNCs was intravenously administered to a 220 g rat and the distribution of the UCNCs was tracked by X-ray CT imaging at timed intervals (Fig. 7). In general, dose requirement was highly dependent on the contrast efficiency of imaging elements. Compared with the previous metal-based nanoparticle contrast agents, the dose of our contrast agent in single injection (denoted as 1 mL of 448 mg Gd per mL per rat weighed 220 g) was applied in terms of the high Gd content in a single 4-layer $NaYF_4$:Yb, Er@$NaGdF_4$ nanoparticle. An enhancement of the signal of the heart could be observed at least within 15 minutes without an appreciable loss of contrast. After 15 minutes, the enhancement of the signal of the heart and vascular tissue decreased rapidly (Fig. 7b, Table S1 in the ESI†). Long-lasting circulation in vessels is a key factor in many biomedical applications, including vascular imaging and diagnosis of diseases. However, the gradual enhancement (Fig. 7a and b) of the signals of the liver and spleen continued for over one and a half hours. A more careful view at the 3D-renderings of CT images (Fig. 7c and d)

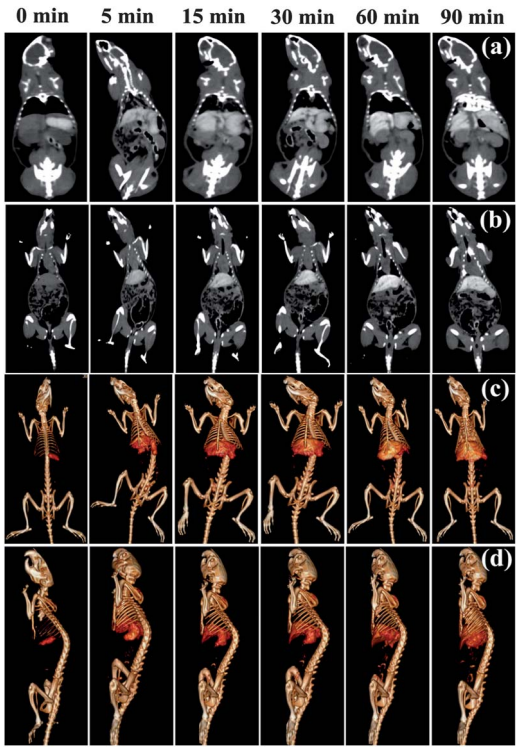

Fig. 7 *In vivo* CT coronal view images of a rat after intravenous injection of 1 mL of 4-layer $NaYF_4$:Yb, Er@$NaGdF_4$ core–shell UCNC (448 Gd mg mL^{-1}) solution at timed intervals. (a) Spleen and kidney. (b) Liver. (c) The corresponding liver's 3D renderings of *in vivo* CT images. (d) Spleen and kidney's renderings of *in vivo* CT images.

shows evident enhancement of the signals of great vessels within the same period of time as well. This long-lasting liver-signal enhancement may improve the detection of the hepatic metastases.[57,58]

For comparison, we also imaged a different rat after intravenous administration of Iobitridol using the same CT protocol (Fig. S5 and Table S2 in the ESI†). Quick imaging five minutes after injection confirmed that most of the Iobitridol had accumulated in the urinary organs (kidney and bladder), and no contrast was detected in other organs, thereby indicating the short circulation time and rapid vascular permeation of Iobitridol. These inherent limitations of Iobitridol also made it unsuitable for lymph node delivery to improve cancer staging, which would be helpful in avoiding unnecessary surgery. This result demonstrates that $NaYF_4$:Yb, Er@$NaGdF_4$ layer-by-layer core–shell UCNCs could be good agents as CT imaging probes for *in vivo* cancer treatment.

4 Conclusions

In summary, we have, for the first time, synthesized highly water-soluble $NaYF_4$:Yb, Er@$NaGdF_4$ multilayer core–shell UCNCs by a microwave-assisted route. In contrast to previous observations, we proposed a strategy to enhance the intensity of NIR-to-visible upconversion in Ln^{3+}-doped nanocrystals by employing a layer-by-layer core–shell architecture. The phase transition from cubic to cubic-hexagonal by fine-tuning $NaGdF_4$

shells coated on $NaYF_4$:Yb, Er cores led to a significant increase in particle size, from 16.3 nm to about 30.6 nm. Moreover, the up-down conversion dual-mode luminescent $NaYF_4$:Yb, Er@$NaGdF_4$:Ce, Ln (Eu, Tb, Sm, Dy) nanocrystals were also established to further validate the successful formation of a core–shell structure. The feasibility of prepared $NaYF_4$:Yb, Er@$NaGdF_4$ core–shell UCNCs as *in vivo* CT contrast agents was intensively investigated, and the results revealed that core–shell UCNCs showed low cytotoxicity and long circulation time *in vivo*. More significantly, multilayer core–shell UCNCs provided a much higher efficacy compared to the monolayer core–shell agent. This multimodal imaging property would allow these nanocrystals to provide a better reliability of the collected data and have great potential in biological and medical applications.

Acknowledgements

This work was supported by the Foundation of the National Natural Science Foundation of China (no. 20971054, 90922034 and 21131002), Specialized Research Fund for the Doctoral Program of Higher Education (no. 20110061110015), National High Technology Research and Develop Program (863 program) of China (no. 2013AA031702) and the Special Program of China Postdoctoral Science Foundation (no. 2012T50288). X. G. Kong would like to thank the NSF of china (no.11174277 and 61275202). ESI is available online from Wiley InterScience or from the author.

Notes and references

1 S. W. Wua, G. Hana, D. J. Millirona, S. Alonia, V. Altoea, D. V. Talapinb, B. E. Cohena and P. J. Schuck, *Proc. Natl. Acad. Sci. U. S. A.*, 2009, **106**, 10917.
2 V. P. Chauhan, Z. Popovic, O. Chen, J. Cui, D. Fukumura, M. G. Bawendi and R. K. Jain, *Angew. Chem., Int. Ed.*, 2011, **50**, 11417.
3 M. Q. Zhu, G. F. Zhang, C. Li, M. P. Aldred, E. Chang, R. A. Drezek and A. D. Q. Li, *J. Am. Chem. Soc.*, 2011, **133**, 365.
4 Z. Q. Li, Y. Zhang and S. Jiang, *Adv. Mater.*, 2008, **20**, 4765.
5 X. X. He, K. M. Wang and Z. Cheng, *Adv. Rev.*, 2010, **2**, 349.
6 H. Kobayashi, Y. Koyama, T. Barrett, Y. Hama, C. A. S. Regino, I. S. Shin, B. S. Jang, N. Le, C. H. Paik, P. L. Choyke and Y. Urano, *ACS Nano*, 2007, **1**, 258.
7 J. M. Luther, P. K. Jain, T. Ewers and A. P. Alivisatos, *Nat. Mater.*, 2011, **10**, 361.
8 E. H. Sargent, *Nat. Photonics*, 2012, **6**, 133.
9 D. Zhitomirsky, M. Furukawa, J. Tang, P. Stadler, S. Hoogland, O. Voznyy, H. Liu and E. H. Sargent, *Adv. Mater.*, 2012, **24**, 6181.
10 Z. A. Peng and X. G. Peng, *J. Am. Chem. Soc.*, 2001, **123**, 183.
11 Z. L. Cheng, A. A. Zaki, J. Z. Hui, V. R. Muzykantov and A. Tsourkas, *Science*, 2012, **338**, 903.
12 S. Ghaderi, B. Ramesh and A. M. Seifalian, *J. Drug Targeting*, 2011, **19**, 475.
13 L. Ye, K. T. Yong, L. W. Liu, I. Roy, R. Hu, J. Zhu, H. X. Cai, W. C. Law, J. W. Liu, K. Wang, J. Liu, Y. Q. Liu, Y. Z. Hu, X. H. Zhang, M. T. Swihart and P. N. Prasad, *Nat. Nanotechnol.*, 2012, **7**, 453.
14 G. Tikhomirov, S. Hoogland, P. E. Lee, A. Fischer, E. H. Sargent and S. O. Kelley, *Nat. Nanotechnol.*, 2011, **6**, 485.
15 S. Kim, Y. Taik Lim, E. G. Soltesz, A. M. D. Grand, J. Lee, A. Nakayama, J. A. Parker, T. Mihaljevic, R. G. Laurence, D. M. Dor, L. H. Cohn, M. G. Bawendi and J. V. Frangioni, *Nat. Biotechnol.*, 2004, **22**, 93.
16 (*a*) J. Wang, F. Wang, C. Wang, Z. Liu and X. G. Liu, *Angew. Chem., Int. Ed.*, 2011, **50**, 10369; (*b*) Z. Liu, Z. H. Li, J. H. Liu, S. Gu, Q. H. Yuan, J. S. Ren and X. G. Qu, *Biomaterials*, 2012, **33**, 6748.
17 Z. Q. Li and Y. Zhang, *Angew. Chem., Int. Ed.*, 2006, **45**, 7732.
18 L. H. Fischer, G. S. Harms and O. S. Wolfbeis, *Angew. Chem., Int. Ed.*, 2011, **50**, 4546.
19 (*a*) J. H. Zeng, J. Su, Z. H. Li, R. X. Yan and Y. D. Li, *Adv. Mater.*, 2005, **17**, 2119; (*b*) Z. Liu, F. Pu, S. Huang, Q. H. Yuan, J. S. Ren and X. G. Qu, *Biomaterials*, 2013, **34**, 1712.
20 F. Wang and X. G. Liu, *Chem. Soc. Rev.*, 2009, **38**, 976.
21 Z. Y. Hou, C. X. Li, P. A. Ma, Z. Y. Cheng, X. J. Li, X. Zhang, Y. L. Dai, D. M. Yang, H. Z. Lian and J. Lin, *Adv. Funct. Mater.*, 2012, **22**, 2713.
22 J. Zhou, Z. Liu and F. Y. Li, *Chem. Soc. Rev.*, 2012, **41**, 1323.
23 L. Cheng, K. Yang, Y. G. Li, X. Zeng, M. W. Shao, S. T. Lee and Z. Liu, *Biomaterials*, 2012, **33**, 2215.
24 Q. Q. Zhan, J. Qian, H. J. Liang, G. Somesfalean, D. Wang, S. L. He, Z. G. Zhang and S. Andersson-Engels, *ACS Nano*, 2011, **5**, 3744.
25 (*a*) D. K. Chatterjeea, A. J. Rufaihaha and Y. Zhang, *Biomaterials*, 2008, **29**, 937; (*b*) Z. Liu, F. Pu, J. H. Liu, L. Y. Jiang, Q. H. Yuan, Z. Q. Li, J. S. Ren and X. G. Qu, *Nanoscale*, 2013, **5**, 4252.
26 X. C. Yea, J. E. Collinsb, Y. Kanga, J. Chenc, D. T. N. Chend, A. G. Yodhd and C. B. Murray, *Proc. Natl. Acad. Sci. U. S. A.*, 2010, **107**, 22430.
27 Z. Wang, C. H. Liu, L. J. Chang and Z. P. Li, *J. Mater. Chem.*, 2012, **22**, 12186.
28 C. H. Dong, A. Korinek, B. Blasiak, B. Tomanek and F. C. J. M. van Veggel, *Chem. Mater.*, 2012, **24**, 1297.
29 F. Wang and X. G. Liu, *J. Am. Chem. Soc.*, 2008, **130**, 5642.
30 K. A. Abel, J. C. Boyer and F. C. J. M. van Veggel, *J. Am. Chem. Soc.*, 2009, **131**, 14644.
31 G. Y. Chen, T. Y. Ohulchanskyy, W. C. Law, H. Agren and P. N. Prasad, *Nanoscale*, 2011, **3**, 2003.
32 F. Wang, J. Wang and X. G. Liu, *Angew. Chem., Int. Ed.*, 2010, **49**, 7456.
33 H. S. Qian and Y. Zhang, *Langmuir*, 2008, **24**, 12123.
34 A. D. Ostrowski, E. M. Chan, D. J. Gargas, E. M. Katz, G. Han, P. J. Schuck, D. J. Milliron and B. E. Cohen, *ACS Nano*, 2012, **6**, 2686.
35 X. M. Liu, X. G. Kong, Y. L. Zhang, L. P. Tu, Y. Wang, Q. H. Zeng, C. G. Li, Z. Shi and H. Zhang, *Chem. Commun.*, 2011, **47**, 11957.
36 F. Chen, W. B. Bu, S. J. Zhang, X. H. Liu, J. N. Liu, H. Y. Xing, Q. F. Xiao, L. P. Zhou, W. J. Peng, L. Z. Wang and J. L. Shi, *Adv. Funct. Mater.*, 2011, **21**, 4285.

37 Y. S. Liu, D. T. Tu, H. M. Zhu, R. F. Li, W. Q. Luo and X. Y. Chen, *Adv. Mater.*, 2010, **22**, 3266.
38 F. Vetrone, R. Naccache, V. Mahalingam, C. G. Morgan and J. A. Capobianco, *Adv. Funct. Mater.*, 2009, **19**, 2924.
39 N. J. J. Johnson, A. Korinek, C. H. Dong and F. C. J. M. van Veggel, *J. Am. Chem. Soc.*, 2012, **134**, 11068.
40 X. M. Li, D. K. Shen, J. P. Yang, C. Yao, R. C. Che, F. Zhang and D. Y. Zhao, *Chem. Mater.*, 2013, **25**, 106.
41 F. F. Li, C. G. Li, X. M. Liu, Y. Chen, T. Y. Bai, L. Wang, Z. Shi and S. H. Feng, *Chem.–Eur. J.*, 2012, **18**, 11641.
42 F. Wang, X. P. Fan, M. Q. Wang and Y. Zhang, *Nanotechnology*, 2007, **18**, 025701.
43 Q. Q. Su, S. Y. Han, X. J. Xie, H. M. Zhu, H. Y. Chen, C. K. Chen, R. S. Liu, X. Y. Chen, F. Wang and X. G. Liu, *J. Am. Chem. Soc.*, 2012, **134**, 20849.
44 H. X. Mai, Y. W. Zhang, L. D. Sun and C. H. Yan, *J. Phys. Chem. C*, 2007, **111**, 13721.
45 Q. Q. Dou, N. M. Idris and Y. Zhang, *Biomaterials*, 2013, **34**, 1722.
46 D. Q. Chen, L. Lei, A. P. Yang, Z. X. Wang and Y. S. Wang, *Chem. Commun.*, 2012, **48**, 5898.
47 G. S. Yi and G. M. Chow, *Chem. Mater.*, 2007, **19**, 341.
48 F. Zhang, R. C. Che, X. M. Li, C. Yao, J. P. Yang, D. K. Shen, P. Hu, W. Li and D. Y. Zhao, *Nano Lett.*, 2012, **12**, 2852.
49 F. Wang, R. R. Deng, J. Wang, Q. X. Wang, Y. Han, H. M. Zhu, X. Y. Chen and X. G. Liu, *Nat. Mater.*, 2011, **10**, 968.
50 F. Wang, Y. Han, C. S. Lim, Y. H. Lu, J. Wang, J. Xu, H. Y. Chen, C. Zhang, M. H. Hong and X. G. Liu, *Nat. Mater.*, 2010, **463**, 1061.
51 F. F. Li, C. G. Li, X. M. Liu, T. Y. Bai, W. J. Dong, X. Zhang, Z. Shi and S. H. Feng, *Dalton Trans.*, 2013, **42**, 2015.
52 Y. Wang, K. Liu, X. M. Liu, K. Dohnalova, T. Gregorkiewicz, X. G. Kong, M. C. G. Aalders, W. J. Buma and H. Zhang, *J. Phys. Chem. Lett.*, 2011, **2**, 2083.
53 D. Q. Chen, Y. L. Yu, F. Huang, A. P. Yang and Y. S. Wang, *J. Mater. Chem.*, 2011, **21**, 6186.
54 C. G. Li, F. F. Li, T. Li, T. Y. Bai, L. Wang, Z. Shi and S. H. Feng, *Dalton Trans.*, 2012, **41**, 4890.
55 S. J. Zeng, M. K. Tsang, C. F. Chan, K. L. Wong, B. Feid and J. H. Hao, *Nanoscale*, 2012, **4**, 5118.
56 Z. L. Wang, J. H. Hao, H. L. W. Chan, W. T. Wong and K. L. Wong, *Small*, 2012, **8**, 1863.
57 Y. L. Liu, K. L. Ai, J. H. Liu, Q. H. Yuan, Y. Y. He and L. H. Lu, *Angew. Chem., Int. Ed.*, 2012, **51**, 1437.
58 D. Kim, S. Park, J. H. Lee, Y. Y. Jeong and S. Y. Jon, *J. Am. Chem. Soc.*, 2007, **129**, 7661.